

Supplementary Information

Emerging disorder in $\text{Gd}_2(\text{Ti}_{1-x}\text{Zr}_x)_2\text{O}_7$ pyrochlores matrices for radioactive waste disposal: symmetry lowering versus defect clustering

Armando di Biase ^{*a}, Carlo Castellano ^{*a}, Giorgia Confalonieri ^b, Patrizia Fumagalli ^c, Simone Tumati ^c, Davide Ceresoli ^d and Marco Scavini ^{*a, e}

^a Dipartimento di Chimica, Università degli Studi di Milano, via Golgi 19, 20131 Milano, Italy. E-mail armando.dibiase@unimi.it, carlo.castellano@unimi.it, marco.scavini@unimi.it.

^b ESRF- European Synchrotron Research Facility, 71 avenue des Martyrs, 38043 Grenoble, France.

^c Dipartimento di Scienze della Terra, Università degli Studi di Milano, via Botticelli 23, 20133 Milano, Italy.

^d Istituto di Scienze e Tecnologie Chimiche "Giulio Natta" (SCITEC), Consiglio Nazionale delle Ricerche (CNR), PST via Fantoli 16/15, 20138 Milan and via Golgi 19, Milano 20133, Italy.

^e Consorzio Interuniversitario Nazionale per la Scienza e Tecnologia dei Materiali (INSTM), Via Giusti 9, 50121, Firenze, Italy

Index

| | |
|--|----|
| Size and strain analysis | 2 |
| Phase inhomogeneity | 4 |
| Pyrochlore model and results from Rietveld refinements | 5 |
| Raman features | 6 |
| PDF analysis results | 9 |
| Structures from DFT calculations | 11 |
| References | 13 |

Size and strain analysis

The experimental patterns of $x_{Zr}=0.75$ (Panel A) and $x_{Zr}=0.85$ (Panel B) samples (already shown in figure 1 of the main text,) are displayed in Figure S1 as black circles for sake of clearness. To reveal the compounds microstructure, the experimental peaks up to $2\theta=20^\circ$ ($Q_{max}\approx 6 \text{ \AA}^{-1}$) were fitted using Pseudo-Voigt functions and after the deconvolution of the instrumental resolution function, as described in the instrumental section, their integral breaths were plotted according to the W.-H. equation, to calculate the crystallite size (D_V) and strain (ϵ) contribution to peak broadening.

In the insets of Figure S11 the W-H plots for the $x_{Zr}=0.75$ (Panel A) and $x_{Zr}=0.85$ (Panel B) samples are reported. The experimental $\beta\cos\theta$ data for the *fluorite* peaks are represented by full circles, while the *pyrochlore* (*superstructure*) ones are depicted as empty circles.

Up to $x=0.75$, all the experimental points lie on the same straight line. For $x\geq 0.85$, the empty circles are systematically shift toward higher values pointing to a reduced crystallographic coherence of pyrochlore ordering in respect to the crystallite size. so that two linear regression lines have to be used (see inset of Fig.S11 panel B). It is worth noting that the two interpolating lines are almost parallel to each other, so affecting the D_V value rather than the ϵ one. The calculated ϵ and λ/D_V values are shown in Figure SI panel C and D respectively. Strain ϵ is almost 10^{-4} for $x=0$, as expected for a well grown crystalline phase; then it suddenly grows up of an order of magnitude in the $x=0.15$ sample and smoothly decreases on raising x_{Zr} , reaching $\approx 8 \times 10^{-4}$ in the Ti-free sample. This behavior suggests that all intermediate compositions in the $Gd_2(Ti_{1-x}Zr_x)_2O_7$ solid solution and the $Gd_2Zr_2O_7$ endmember are much more disordered than the $Gd_2Ti_2O_7$ endmember. λ/D_V values are very close to zero, testifying the micrometric size of the crystallites of all the samples. We prefer to plot this parameter instead of the particle dimension D_V because the inverse proportionality between them would generate enormous $\sigma(D_V)$ values and confuse the reader. Also, in Figure SI panel D the empty circles refer to the fitted parameters of the pyrochlore superstructure peaks. The shift toward larger λ/D_V values in respect to the fluorite peaks could indicate a slightly lower structure coherence: some lowering of the pyrochlore ordering in respect to the whole crystallites.

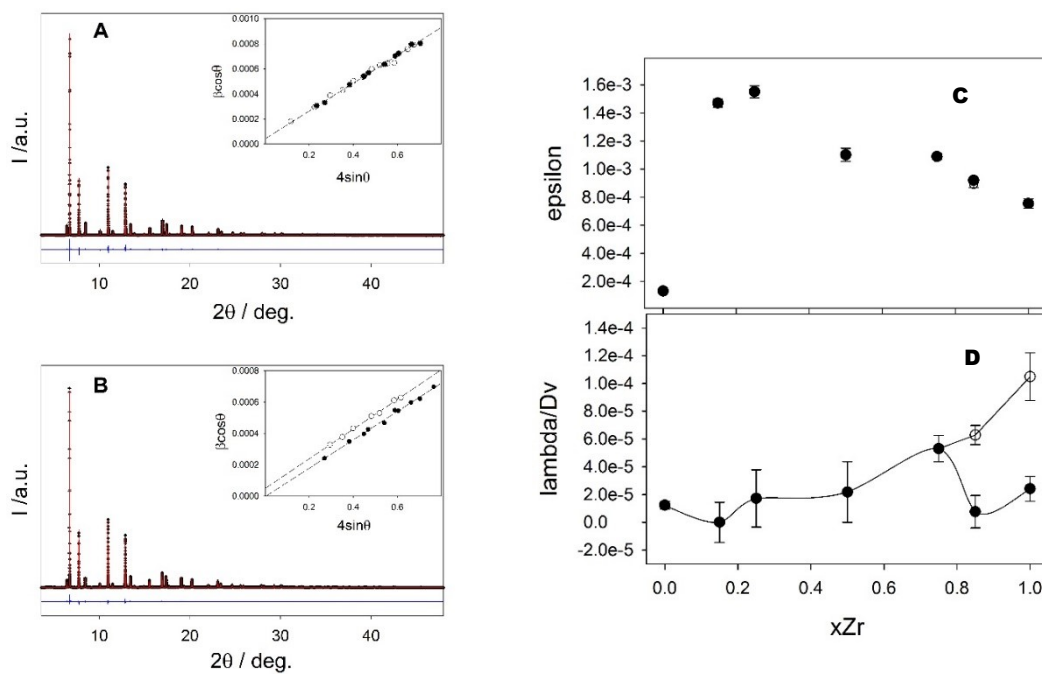


Figure SI1. HR-XRPD patterns of $\text{Gd}_2(\text{Ti}_{1-x}\text{Zr}_x)_2\text{O}_7$ for $x\text{Zr} = 0.75$ (A) and 0.85 (B) with corresponding W.H. plots in the insets. The calculated strain (ϵ) values and λ/D_v values are shown in panels (C) and (D), respectively. Full and empty circles are the refined values for the *fluorite* and *pyrochlore* peaks, respectively.

Phase inhomogeneity

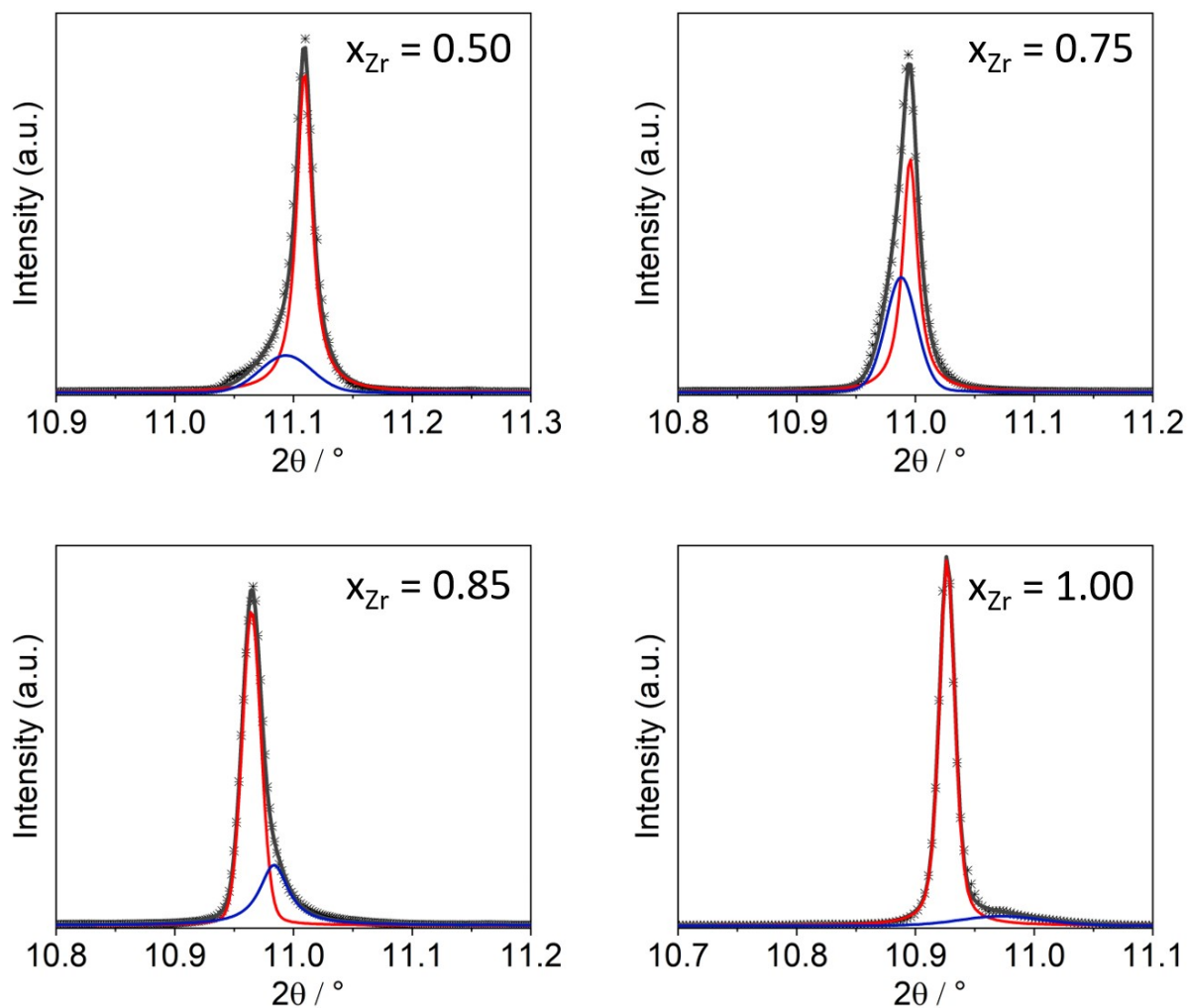


Figure SI2. Close-up view of (440)_p reflection in selected HR-XRPD patterns of Gd₂(Ti_{1-x}Zr_x)₂O₇ solid solution. Cross symbols represent the observed pattern; the dark grey solid line is the total calculated profile by Rietveld refinement, while solid red and blue lines are the calculated profile for Phase 1 and Phase 2 respectively.

Pyrochlore model and results from Rietveld refinements

Table S11 Pyrochlore structural model employed in Rietveld refinements of HR-XRPD patterns (s.g. $Fd\bar{3}m$, n°227, origin choice 2, origin at the B site)

| Atom | Wyckoff letter | x | y | z |
|------|----------------|---------------|---------------|---------------|
| A | $16d$ | $\frac{1}{2}$ | $\frac{1}{2}$ | $\frac{1}{2}$ |
| B | $16c$ | 0 | 0 | 0 |
| O1 | $48f$ | x^a | $\frac{1}{8}$ | $\frac{1}{8}$ |
| O2 | $8b$ | $\frac{3}{8}$ | $\frac{3}{8}$ | $\frac{3}{8}$ |
| O3 | $8a$ | $\frac{1}{8}$ | $\frac{1}{8}$ | $\frac{1}{8}$ |

^a xO1 ranges from 0.3260 in $Gd_2Ti_2O_7$ to 0.3470 in $Gd_2Zr_2O_7$

Table S12 Structural parameters extracted from Rietveld refinements of HR-XRPD patterns

| xZr | | 0 | 0.15 | 0.25 | 0.50 | 0.75 | 0.85 | 1 |
|------------------------|-------------------|--------------|-------------|-------------|-------------|-------------|-------------|-------------|
| Phase 1 | Weight Fraction % | 94.3 | 99.9 | 98.0 | 79.2 | 57.9 | 70.8 | 89.6 |
| | a / Å | 10.178215(8) | 10.23104(3) | 10.26928(3) | 10.35152(2) | 10.45829(3) | 10.48699(3) | 10.52304(2) |
| Phase 2 | Weight Fraction % | 5.7 | 0.01 | 2.0 | 20.7 | 42.1 | 29.2 | 10.4 |
| | a / Å | 10.232(3) | 10.42(2) | 10.3372(8) | 10.3659(2) | 10.46544(6) | 10.4690(1) | 10.4790(6) |
| xO1 | | 0.3260(2) | 0.3279(2) | 0.3294(2) | 0.3337 (2) | 0.3415(2) | 0.3438(2) | 0.34698(4) |
| o.f.(O3) | | 0 | 0.06(1) | 0.08(1) | 0.20(1) | 0.27(1) | 0.338(9) | 0.40(1) |
| o.f.(Zr _A) | | 0 | 0 | 0 | 0 | 0.026(1) | 0.045(1) | 0.048(2) |
| Uiso / Å ² | A | 0.00447(3) | 0.00449(4) | 0.00536(5) | 0.00918 (6) | 0.01198(6) | 0.01203(6) | 0.01135(8) |
| | B | 0.00372(7) | 0.0040(1) | 0.0055(1) | 0.0090(1) | 0.0144(1) | 0.0165(1) | 0.0182(2) |
| | O | 0.0030(3) | 0.0034(4) | 0.0052(5) | 0.0098(6) | 0.0233(7) | 0.0236(6) | 0.0233(9) |
| wRp(%) | | 11.5 | 9.5 | 9.2 | 8.4 | 7.2 | 6.8 | 7.6 |
| Goodness-of-Fit | | 7.9 | 4.3 | 4.5 | 3.9 | 4.5 | 3.0 | 5.5 |

Raman features

Besides the fundamental bands of the pyrochlore structure discussed in the main text, other modes are observed as well. The band at $\approx 115 \text{ cm}^{-1}$ (**M1**) in the spectrum of the Ti-endmember has been already reported in previous investigations on $\text{Gd}_2\text{Ti}_2\text{O}_7$ ^{1,2} and could be ascribed to a lowering of the local symmetry, which activates formally forbidden IR modes³. This evidence suggests that although the $\text{Gd}_2\text{Ti}_2\text{O}_7$ approaches the ideal pyrochlore structure more than any composition in this study, some degree of distortion is retained. The progressive substitution of Zr in the structure enhances the distortion and deviation from the ideal pyrochlore structure and leads to a relaxation of the selection rules. Moving on to the line at $\approx 215 \text{ cm}^{-1}$ (**M2**), this has been assigned to one of the four T_{2g} modes by several authors^{1,4-6} and related to the vibration of O2 at the center of OGd_4 tetrahedra¹. The decrease in intensity with Zr-substitution may be ascribed to a change in the position of O2 and/or distortion of the corresponding OGd_4 tetrahedron. A similar trend was observed in the case of pressure induced distortion in $\text{Gd}_2\text{Ti}_2\text{O}_7$ ⁵. Kumar and coworkers showed by means of DFT calculations that no Raman active modes should be allowed below 220 cm^{-1} and it is likely that the **M2** line is another forbidden IR mode activated by displacive disorder of Gd and O2 ions^{7,8}. The band at $\approx 258 \text{ cm}^{-1}$, which is hardly visible in the spectrum of $\text{Gd}_2\text{Ti}_2\text{O}_7$ and completely disappears in the other spectra of the solid solution, has been assigned to a T_{2g} mode by Lummen and coworkers¹. The other weak feature in the spectrum of $\text{Gd}_2\text{Ti}_2\text{O}_7$ is the band $\approx 450 \text{ cm}^{-1}$ (**M4**), which could be assigned again to one of the remaining T_{2g} modes^{4,6,9}. Kumar and coworkers predicted this mode with contributions of Gd-O2 stretching and O1-Gd-O2 bending force constants in addition to the dominant O1-Ti-O1 bending force constant from TiO_6 octahedra⁷. The band was already observed in $\text{Gd}_2\text{Ti}_2\text{O}_7$ ¹⁰ and other lanthanide titanates $\text{Ln}_2\text{Ti}_2\text{O}_7$ with Ln = Dy, Lu¹¹ and Tb¹². Oueslati and coworkers assigned the **M4** band to B-O vibration and the red-shift with increasing x_{Zr} was regarded as a clear indication of lighter Ti^{4+} being substituted by heavier Zr^{4+} in the structure¹³. A wavenumber of $\approx 400 \text{ cm}^{-1}$ is reached in $\text{Gd}_2\text{Zr}_2\text{O}_7$ for **M4** and similar values were recorded for the same composition¹⁴ and other related zirconate pyrochlores like $\text{Nd}_{2-y}\text{Y}_y\text{Zr}_2\text{O}_7$ ¹⁵, $\text{Nd}_{1-x}\text{Dy}_x\text{Zr}_2\text{O}_7$ ¹⁶ and $\text{Sm}_2\text{Zr}_2\text{O}_7$ ¹⁷.

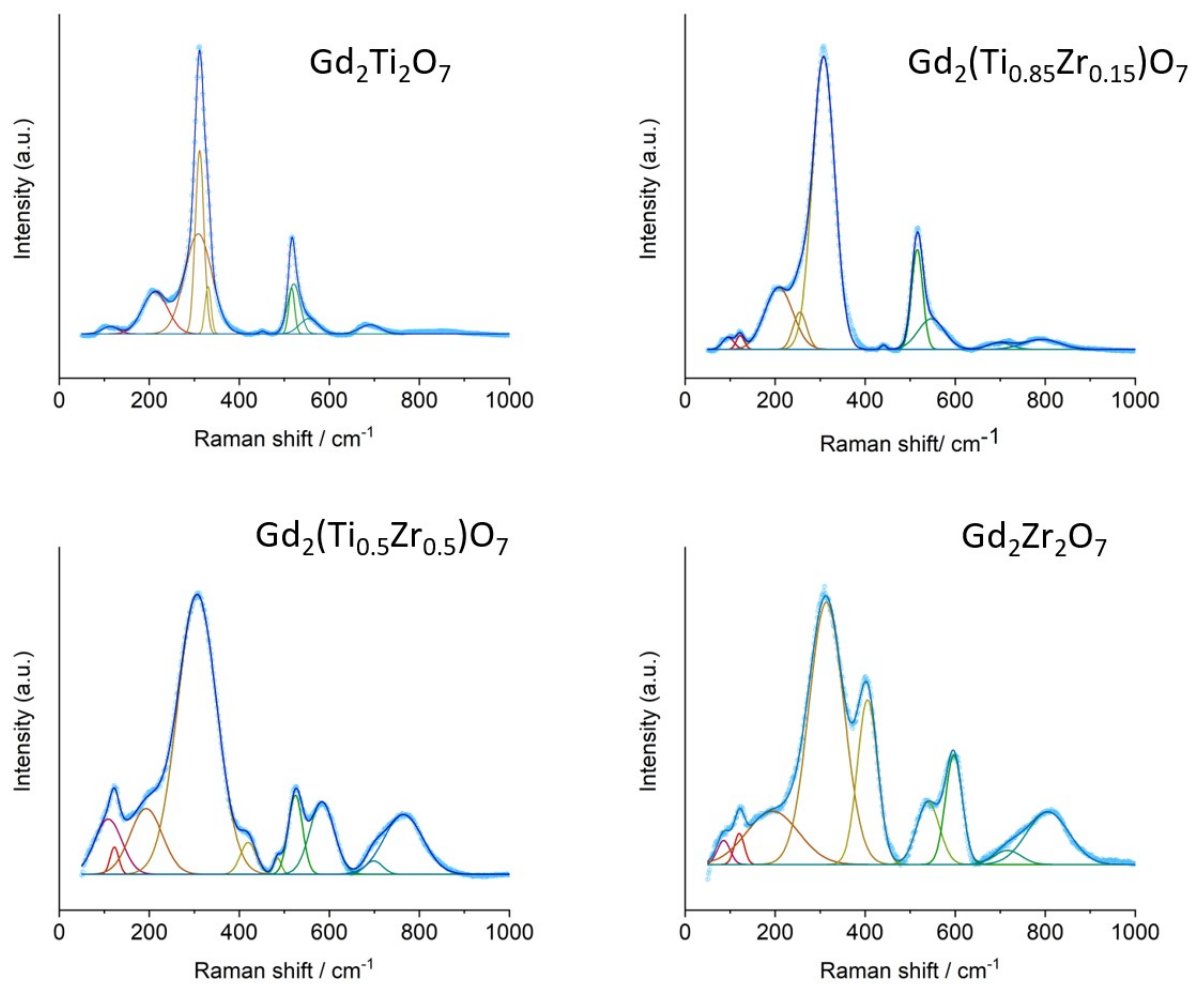


Figure S13 Selected fits for the Raman spectra of $Gd_2(Ti_{1-x}Zr_x)_2O_7$ series

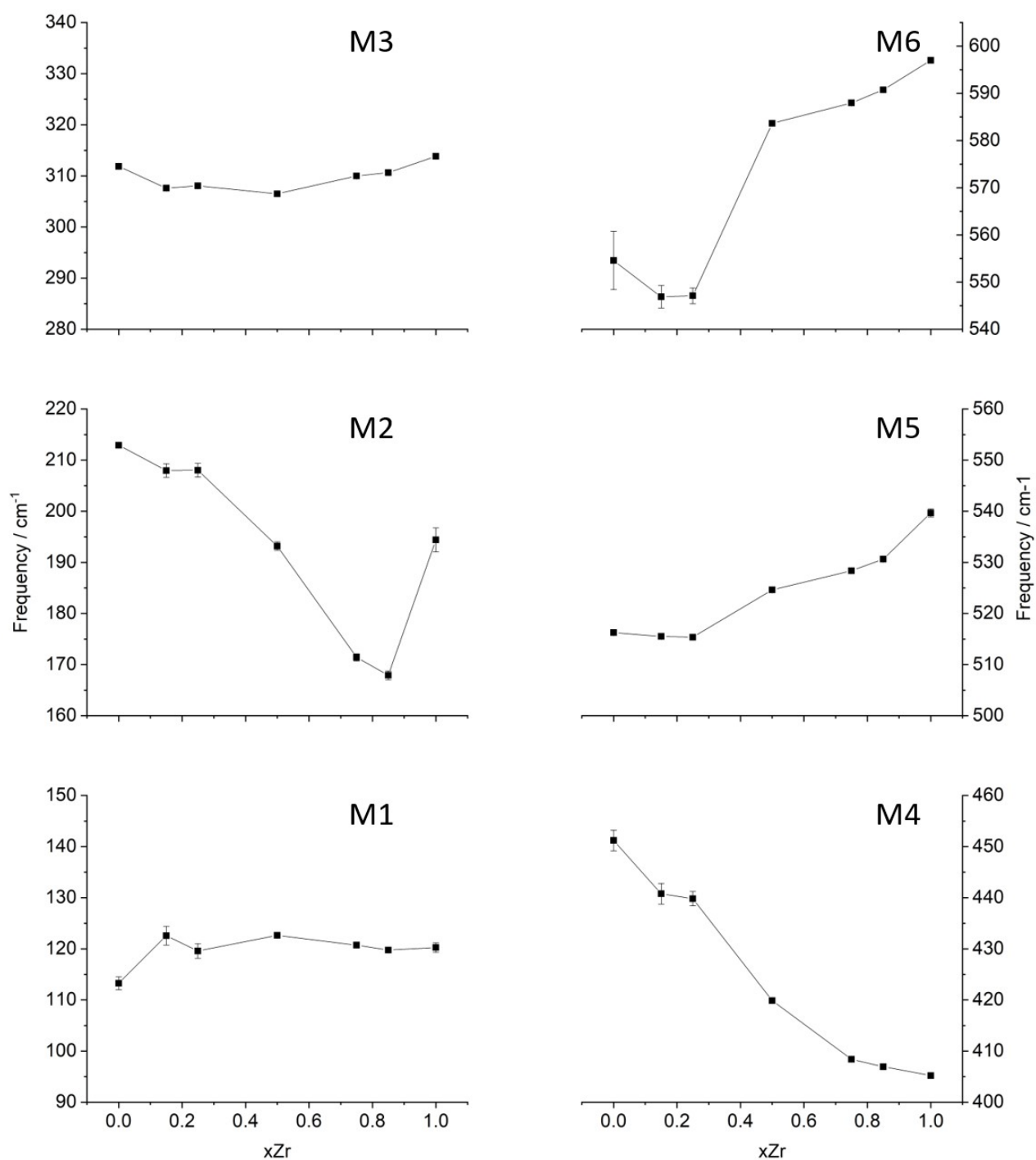


Figure SI4 Frequency shift of Raman modes in $Gd_2(Ti_{1-x}Zr_x)_2O_7$ as obtained by fitting the spectra with Gaussian functions.

PDF analysis results

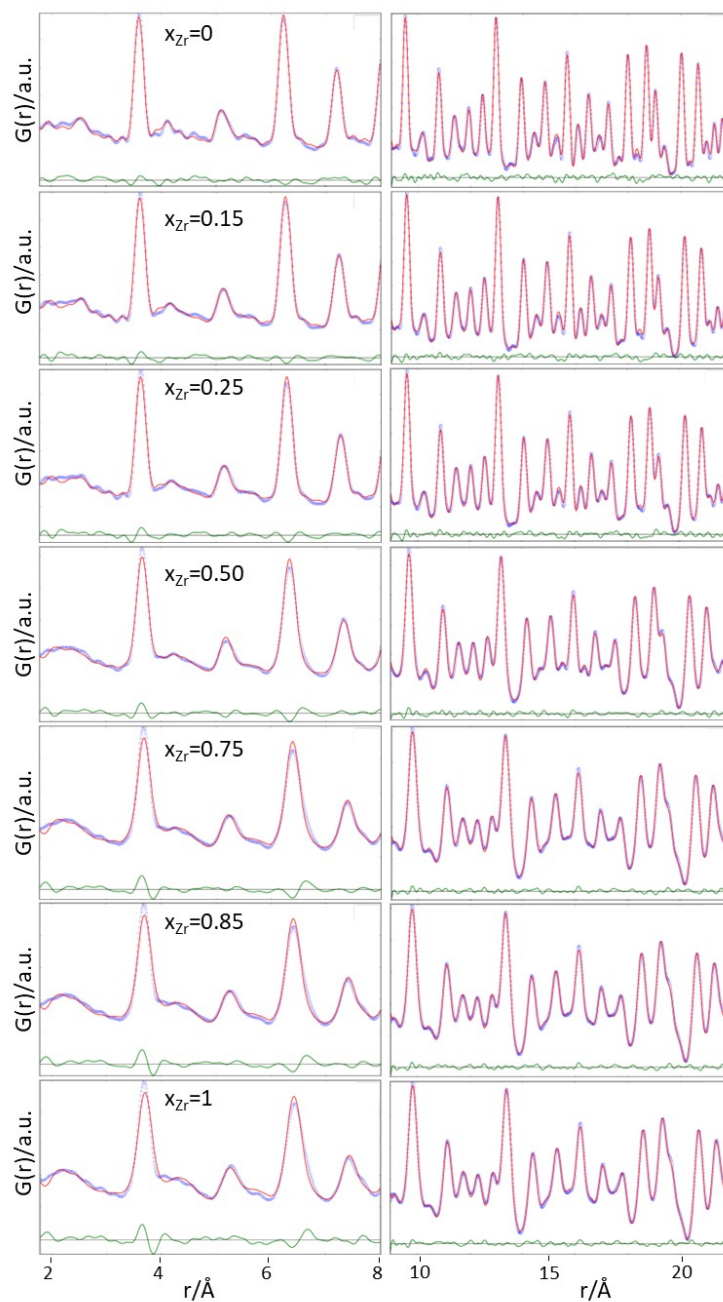


Figure SI5. Experimental $G(r)$ functions in the 1.8-8 \AA (left side) and 9-22 \AA (right side) intervals are displayed as light blue circles. Labels in the panels refer to the sample composition according to $Gd_2(Ti_{1-x}Zr_x)_2O_7$ formula. The fits using the pyrochlore model are reported as red curves. The green curves represent the differences between experimental data and the model-

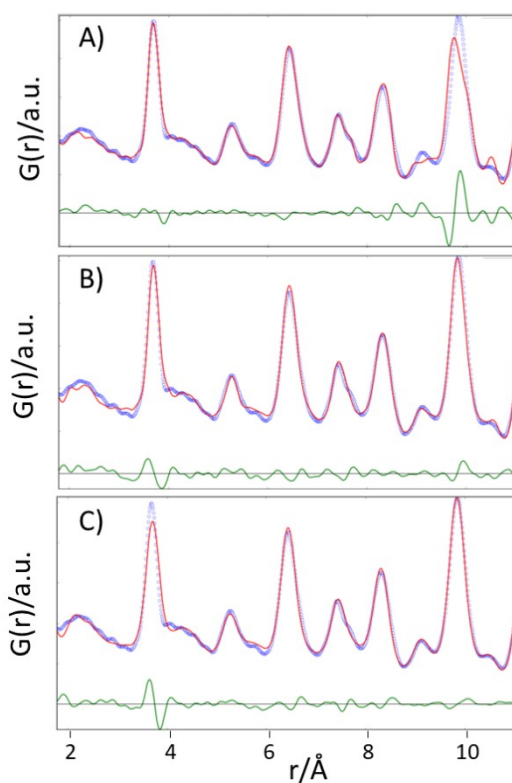


Figure SI6 Fit of the $G(r)$ function pertinent to $Gd_2Zr_2O_7$ sample in the 1.8-11 Å extending the $Pmma$ model fitted in the 1.8-8 range a) without changing the parameters and b) after refinement; panel c) reports the fit using the pyrochlore model.

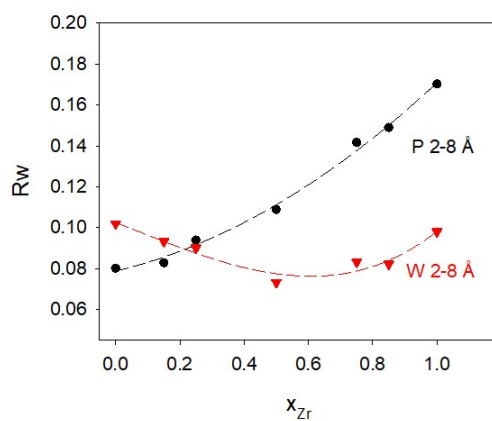


Figure SI7. Residuals of $G(r)$ fits as a function of composition in the 1.8-8 Å range. Black circles refer to pyrochlore structural model, while Red triangles refer to the $Pmma$ weberite-type model. See main text for details.

Structures from DFT calculations

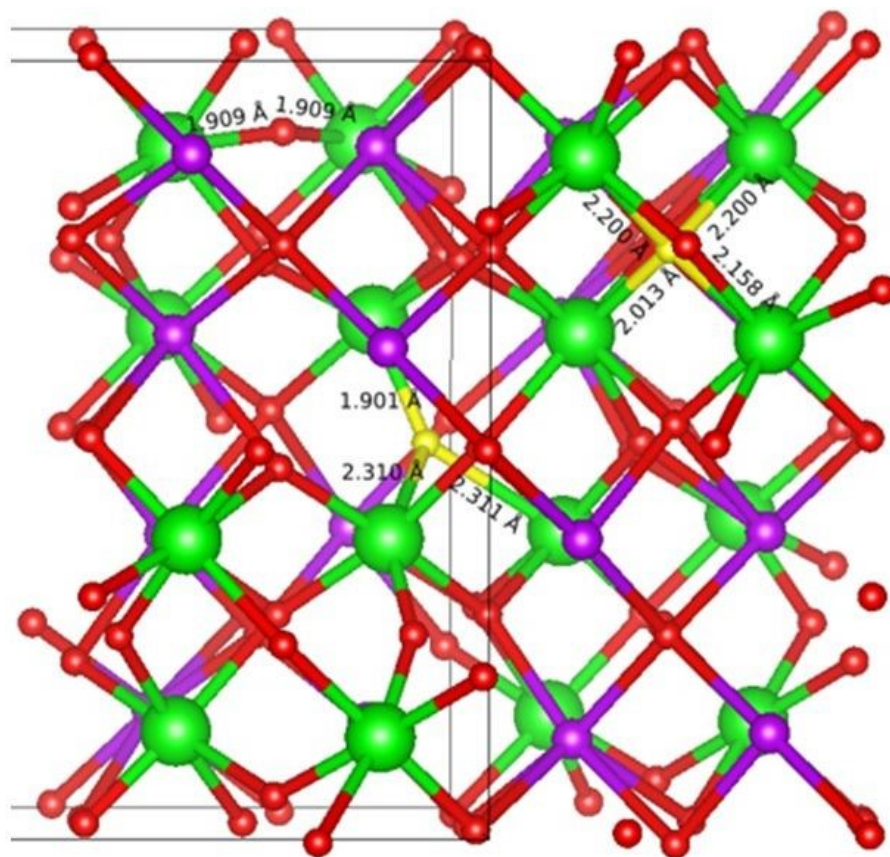


Figure SI8A: Figure_7C enlarged

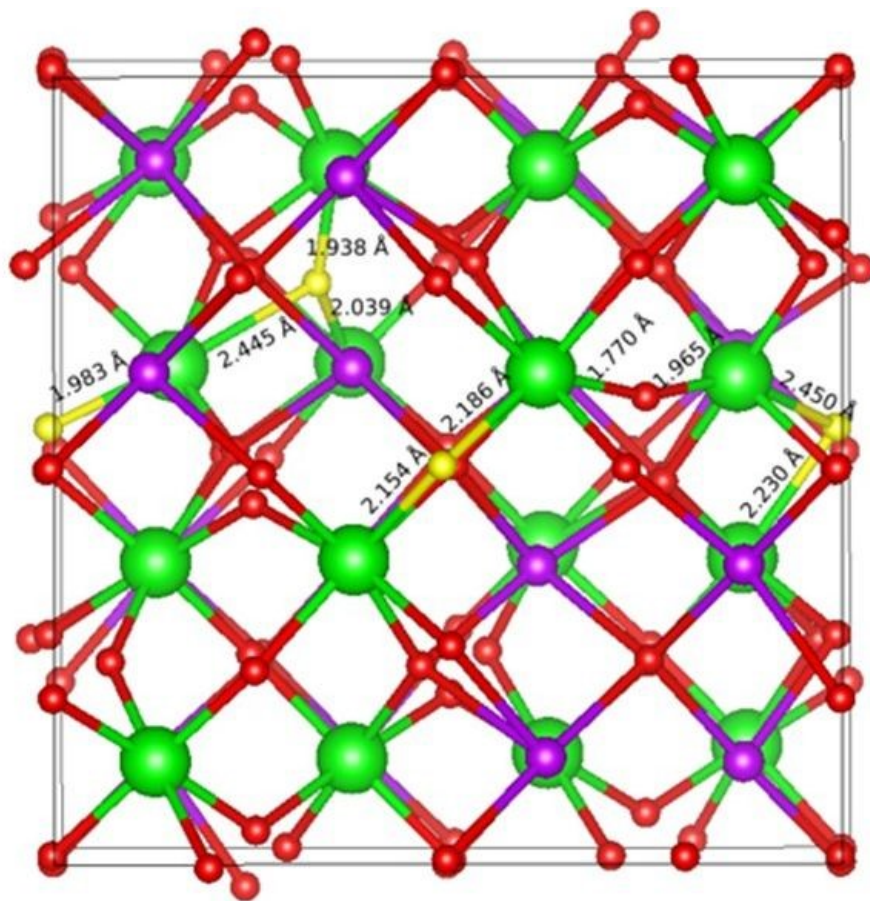


Figure SI8B: Figure_7D enlarged

References

- 1 T. T. A. Lummen, I. P. Handayani, M. C. Donker, D. Fausti, G. Dhalenne, P. Berthet, A. Revcolevschi and P. H. M. Van Loosdrecht, *Phys. Rev. B - Condens. Matter Mater. Phys.*, 2008, **77**, 1–11.
- 2 M. Mori, *Solid State Ionics*, 2003, **158**, 79–90.
- 3 M. T. Vandenborre, E. Husson, J. P. Chatry and D. Michel, *J. Raman Spectrosc.*, 1983, **14**, 63–71.
- 4 N. J. Hess, B. D. Begg, S. D. Conradson, D. E. McCready, P. L. Gassman and W. J. Weber, *J. Phys. Chem. B*, 2002, **106**, 4663–4677.
- 5 S. Saha, D. V. S. Muthu, C. Pascanut, N. Dragoe, R. Suryanarayanan, G. Dhalenne, A. Revcolevschi, S. Karmakar, S. M. Sharma and A. K. Sood, *Phys. Rev. B*, 2006, **74**, 064109.
- 6 M. L. Sanjuán, C. Guglieri, S. Díaz-Moreno, G. Aquilanti, A. F. Fuentes, L. Olivi and J. Chaboy, *Phys. Rev. B*, 2011, **84**, 104207.
- 7 S. Kumar and H. C. Gupta, *Vib. Spectrosc.*, 2012, **62**, 180–187.
- 8 L. Grima, J. I. Peña and M. L. Sanjuán, *J. Alloys Compd.*, 2022, **923**, 166449.
- 9 F. X. Zhang, B. Manoun and S. K. Saxena, *Mater. Lett.*, 2006, **60**, 2773–2776.
- 10 P. K. Kulriya, T. Yao, S. M. Scott, S. Nanda and J. Lian, *J. Nucl. Mater.*, 2017, **487**, 373–379.
- 11 S. Saha, S. Singh, B. Dkhil, S. Dhar, R. Suryanarayanan, G. Dhalenne, A. Revcolevschi and A. K. Sood, *Phys. Rev. B*, 2008, **78**, 214102.
- 12 M. Mączka, J. Hanuza, K. Hermanowicz, A. F. Fuentes, K. Matsuhira and Z. Hiroi, *J. Raman Spectrosc.*, 2008, **39**, 537–544.
- 13 M. Oueslati, M. Balkanski, P. K. Moon and H. L. Tuller, *MRS Proc.*, 1988, **135**, 199.
- 14 M. Jafar, S. B. Phapale, S. Nigam, S. N. Achary, R. Mishra, C. Majumder and A. K. Tyagi, *J. Alloys Compd.*, 2021, **859**, 157781.
- 15 B. P. Mandal, P. S. R. Krishna and A. K. Tyagi, *J. Solid State Chem.*, 2010, **183**, 41–45.
- 16 Z. Yang, Y. Li, W. Pan and C. Wan, *J. Adv. Ceram.*, 2023, **12**, 1001–1014.
- 17 U. A. Renju and P. Prabhakar Rao, *J. Appl. Phys.*, 2019, **126**, 45110.